Hindawi
Advances in Civil Engineering
Volume 2024, Article ID 5501703, 15 pages
https://doi.org/10.1155/2024/5501703

Research Article

Experimental Study on Dynamic Tensile Mechanical Behavior and Fracture Mechanical Characteristics of Sandstone with a Single Prefabricated Fissure

Jie-hao Wu,[1,2,3] **Yu-xiang Du**,[1,2] **Chang-bai Wang**,[3] **and Qi Zong**[3]

[1]*State Key Laboratory of Precision, Wuhan 430056, China*
[2]*Hubei Key Laboratory of Blasting Engineering, Jianghan University, Wuhan 430056, China*
[3]*School of Civil Engineering and Architecture, Anhui University of Science and Technology, Huainan 232001, China*

Correspondence should be addressed to Yu-xiang Du; duyuxiangjh@163.com

Received 16 November 2023; Revised 2 February 2024; Accepted 19 February 2024; Published 12 March 2024

Academic Editor: Chao Zou

The structural stability of engineering rock mass under dynamic disturbance is directly associated with the fracture mechanics properties in engineering practice. Fully understanding the rock's fracture mechanical behavior and crack evolution caused by stress concentration at the crack tip in engineering rock mass under dynamic load can offer useful insight into the rock's dynamic fracture mechanism. A dynamic test using split-Hopkinson pressure bar (SHPB) test system was performed on a single prefabricated fissure sandstone centrally cracked Brazilian disk (CCBD) specimens. Based on the theory of fracture mechanics and one-dimensional stress wave theory, the dynamic crack initiation criterion of CCBD specimen is proposed, and the regression model of sandstone's dynamic fracture toughness under the coupling effect of fissure angle and strain rate is established by using response surface methodology (RSM). The influence of strain rate and fissure angle on stress wave characteristics, dynamic tensile mechanical behavior, and fracture mechanics characteristic was investigated in this study. The findings demonstrate that: (1) The fissure angle plays a pivotal role in determining the failure mode of sandstone. As the fissure angle increases, three distinct failure modes emerge in the sandstone specimens, while variations in strain rate have minimal impact on the fracture mode of these specimens. (2) Alterations in the fissure angle result in changes to the waveform of transmitted waves. When the fissure angle is below 30°, the transmitted wave exhibits "double peak" characteristics; when it exceeds 30°, a "single peak" waveform is observed. This phenomenon can be attributed to diffraction principles governing incident waves. (3) When the impact pressure is 0.2 MPa, the peak load initially exhibits an increase followed by a decrease, with the peak load reaching its maximum at a fracture angle of 60°; when the impact pressures are 0.3 and 0.5 MPa, there exists a negative correlation between the peak load and the fissure angle. (4) The influence of strain rate on sandstone's fracture resistance is predominant, with alterations in fissure angle exerting an auxiliary effect on this property. The research results can provide a theoretical and experimental basis for dynamic disaster prevention in urban underground space.

1. Introduction

During the construction and operation of urban underground projects, various dynamic loads including blasting vibration [1–5], train running vibration [6–12], and mechanical vibration [13–15] will inevitably be imposed on them. These loads can initiate and propagate cracks in the surrounding rock, posing a significant threat to the safety of essential structures such as basements, infrastructure, municipal pipelines, and other urban facilities. Moreover, these vibrations may cause instability in the overall structure. Consequently, there is an increased demand for comprehensive research on the dynamic response of surrounding rock structures.

There exist a wide range of scales for cracks, fissures, and other defects in crustal rocks. The mechanical behavior and failure characteristics of engineering rock masses are primarily influenced by external loads and geometric parameters of internal defects, such as fissure length, fissure angle, and fissure tension [16–19]. Several research studies have examined

the significant influence of fractures on the mechanical properties of jointed rock masses, including their presence, orientation, and angle [20–23]. It has been concluded that under the action of external loads, local stress is concentrated at the crack tip, resulting in crack initiation, expansion, and fracture failure. In order to investigate the fracture characteristics of rock materials, Irwin [24] first used the stress intensity factor K to quantify the strength of the stress field at the crack tip. He further classified fractures into three types (Type I, Type II, and Type III) and introduced a criterion for stress intensity factor in linear elastic fracture mechanics, as $K_i = K_{iC}$ (i = I, II, and III), where K_{iC} represents the fracture toughness. When dealing with dynamic fracture events, the fracture ability of the specimen is characterized by employing the dynamic stress intensity factor K_d. To accurately calculate the stress distribution at the crack tip, it is imperative to replace the equilibrium equation with the equation of motion, thereby taking into account the material's strain rate effect. In recent years, numerous scholars have conducted experiments, numerical simulations, and theoretical analyses to investigate the dynamic fracture mechanical characteristics of fractured rock specimens, resulting in significant research findings. Feng et al. [25] conducted an split-Hopkinson pressure bar (SHPB) impact test to investigate the energy dissipation and debris distribution of rock samples with symmetrical and asymmetrical cross fractures under dynamic loading conditions. Zhang et al. [26] used an SHPB device to examine the influence of various characteristic parameters of single prefabricated cracks on mechanical response and crack evolution in the presence of dynamic disturbances. Yang et al. [27] utilized the discretized virtual internal bond (DVIB) model in conjunction with the element partition method (EPM) to simulate the dynamic fracturing process of rocks containing internal defects under unloading conditions. Their study revealed that as initial stress levels increase, a transition from tension to shear fracture mode occurs. Moreover, when defect inclination angles approach 45° or defects are elongated, shear cracks are more prone to develop. Wu et al. [28] conducted dynamic disturbance tests on cracked straight-through Brazilian disc (CSTBD) granite samples in the mid–low frequency range using the MTS system. The findings of this study revealed a strong correlation between the reduction in fracture toughness and the level of static preloading. Moreover, it was observed that the magnitude of low-frequency disturbances leads to a decrease in strength, while the frequency of disturbances influences the extent of weakening in fracture toughness. Zhao et al. [29] comprehensively reviewed the research findings of numerical and experimental approaches regarding the impact of dynamic loading on fractured rock samples' properties. By considering rock dynamics, damage mechanics, and fracture mechanics perspectives, their study further investigates how fracture characteristics influence mechanical properties, failure modes, and fracture propagation mechanisms under dynamic loads. Dai et al. [30] expanded the application of the cracked chevron notched Brazilian disc (CCNBD) method to dynamic rock fracture testing in order to determine the initial fracture toughness under dynamic loading conditions. Gong et al. [31] utilized an INSTRON testing machine and an enhanced SHPB testing system to conduct a series of dynamic fracture tests on semicircular bend (SCB) marble specimens, proposing a continuous model for the dynamic increase factor of fracture toughness that quantitatively expresses the relationship between loading rate and rock's dynamic fracture toughness. Li et al. [32] conducted a numerical investigation on the dynamic fracture behavior of notched semicircular bend (NSCB) rock specimens with varying notch dip angles. Their findings revealed that the dynamic mixed mode fracture in these specimens was predominantly initiated by microscale tensile damage, and further demonstrated that the resistance to mixed mode fracture was contingent upon the applied loading rate. Wang et al. [33–35] employed the SHPB apparatus to investigate the dynamic fracture toughness of rocks. They utilized three types of specimens, namely hole-cracked flattened Brazilian disc (HCFBD), cracked straight-through flattened Brazilian disc (CSTFBD), and cracked straight-through Brazilian disc (CSTBD). The study aimed to explore the correlation between dynamic fracture toughness and both disc diameter and crack length. Additionally, they examined the relationship between Type I–II composite ratio and pure Type II loading angle as well as specimen size for Type II dynamic fracture toughness analysis. Lu et al. [36] used the SHPB device to apply radial loading on Brazilian disc marble samples containing preexisting cracks and herringbone grooves, enabling an analysis of the dynamic fracture behavior and energy dissipation characteristics during sample failure. Gao et al. [37], utilizing SHPB in conjunction with digital image correlation (DIC) technology and NSCB method, investigated the influence of loading rate on Laurentian granite, examining the relationships between fracture time, fracture toughness, crack growth rate, and loading rate as well as the correlation between fracture toughness and crack growth rate. Shi et al. [19, 38–40] conducted PFC2D simulations revealing that changes in rock material strength parameters are associated with the propagation of microcracks generated under load conditions.

It is evident that the current research on the dynamic fracture mechanical properties of rock materials primarily focuses on investigating the influence of individual factors. However, there are limited findings regarding the combined effect of strain rate and fracture inclination on rock fracture characteristics.

Based on the aforementioned rationale, this study conducted a dynamic splitting test on centrally cracked Brazilian disk (CCBD) specimens made of sandstone. The experiment considered two factors: five fracture dip angles and three impact pressures. The aim was to analyze the influence patterns and mechanisms of these various factors on sandstone failure mode, stress wave waveform, dynamic load radial strain curve, and peak load. Additionally, the study derived a dynamic crack initiation criterion for CCBD specimens based on fracture mechanics theory and one-dimensional stress wave theory. Furthermore, the response surface method (RSM) was employed to establish a regression model for determining the dynamic fracture toughness of sandstone under the combined effect of fracture dip angle and strain rate. An analysis was then conducted to investigate the influence patterns and interactions among different factors. The

Table 1: Physical and mechanical properties of sandstone [41].

Density (g·cm^{-3})	Porosity (%)	Longitudinal wave velocity (m·s^{-1})	Compressive strength (MPa)	Tensile strength (MPa)
2.53	1.47	3,770	118.47	5.52

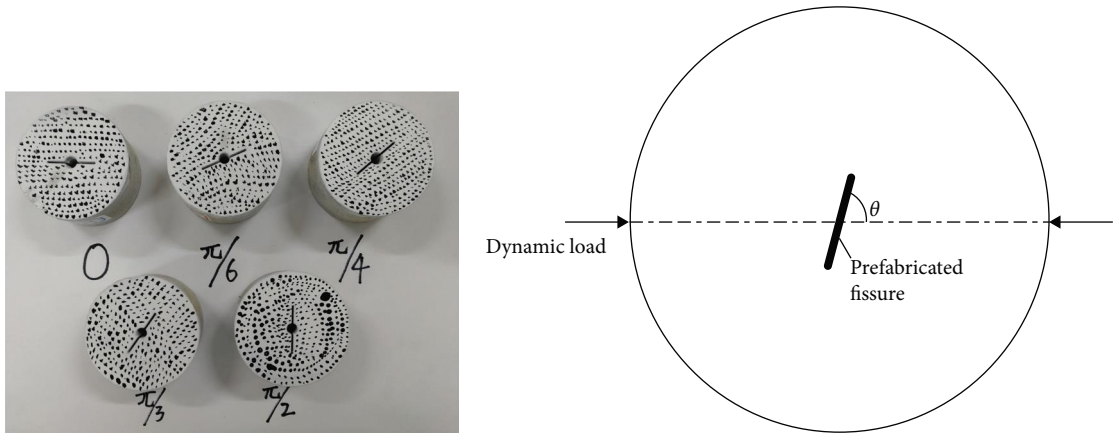

(a) (b)

Figure 1: Sandstone CCBD specimen: (a) the final specimen and (b) the loading state [41].

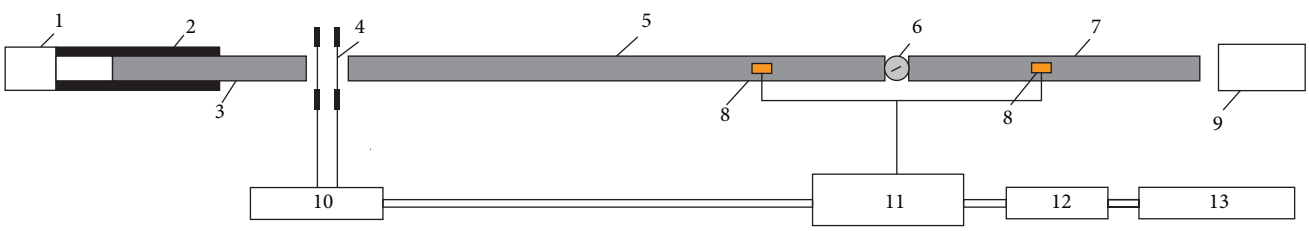

Figure 2: Schematic diagram of SHPB test platform: 1-high-pressure gas chamber, 2-emission cavity, 3-impact bar, 4- laser velocity meter, 5-input bar, 6-specimen, 7-transmission bar, 8-strain gauge, 9-damper, 10-velocity measurement module, 11-ultradynamic strain gauge, 12-oscillograph, and 13-data processing system.

research results provide a deeper understanding of the mechanical properties, fracture propagation behavior, and fracture mechanism of prefractured sandstone under dynamic loads. This study serves as a theoretical and experimental basis for dynamic disaster prevention in urban underground spaces.

2. Impact Splitting Test of Sandstone with a Single Prefabricated Fissure

2.1. Specimen Preparation. The sandstone rock specimens utilized in the experiment were sourced from the excavation roadway situated 880 m below ground level within Zhangji coal mine, located in Huainan city, Anhui province, China. The RWS-200 rock compression rheology testing machine and an ultrasonic detector [41] were employed to characterize the rock specimens. Table 1 presents the physical and mechanical properties of the sandstone.

According to the standards recommended by the International Society for Rock Mechanics and Rock Engineering, Brazilian disc specimens measuring 50 mm in diameter and 25 mm in thickness were fabricated. A high-precision lathe was used to drill a small hole with a diameter of 4 mm at the center of each specimen. Subsequently, the CCBD specimens were successfully processed using the HZWJ2010H/B type CNC ultrahigh pressure water cutting platform from the School of Mechanical Engineering at Anhui University of Science and Technology. The average crack width was measured to be 1.12 mm while the average length reached 20.77 mm. Figure 1 illustrates the final specimen achieved through these procedures and the loading state of the specimen.

2.2. Dynamic Loading System. The test was conducted on the SHPB test platform at the School of Civil Engineering and Architecture, Anhui University of Science and Technology, as shown in Figure 2. The SHPB test platform consists of a power module (including a controller, high-pressure gas chamber, and emission cavity), velocity measurement module (laser velocity meter), signal acquisition module (ultradynamic strain gauge and oscillograph), impact bar, input bar, transmission bar, and damper.

Based on the one-dimensional stress wave theory, when the two ends of the specimen reach a state of stress equilibrium, it can be described as follows:

$$\varepsilon_{\mathrm{I}} + \varepsilon_{\mathrm{R}} = \varepsilon_{\mathrm{T}}, \tag{1}$$

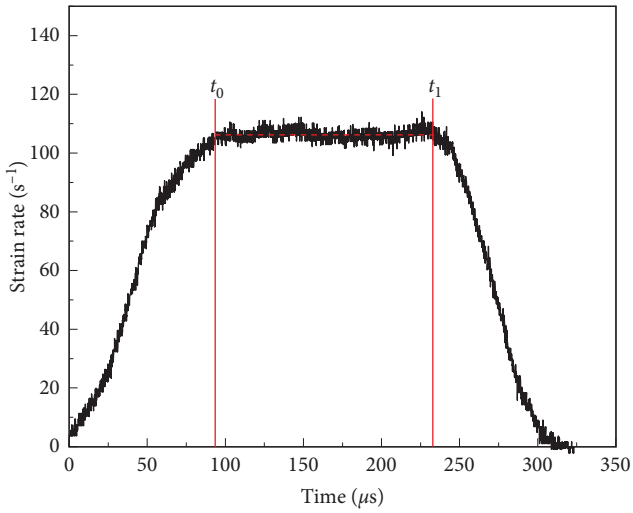

FIGURE 3: Determination of average strain rate in SHPB test.

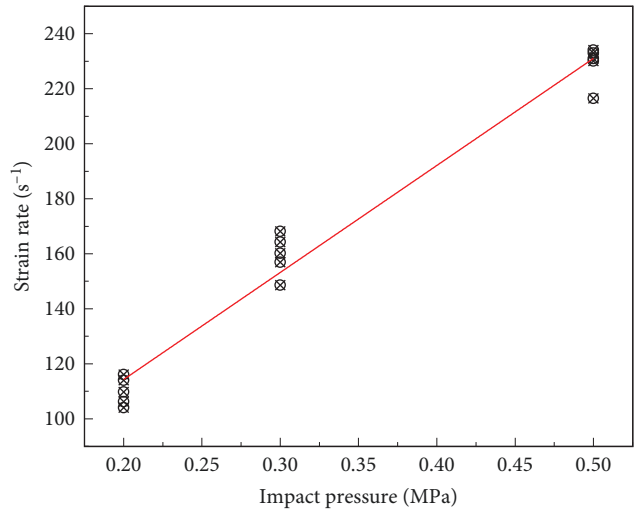

FIGURE 4: Relationship of the impact pressure and the strain rate of CCBD sandstone.

where ε_I, ε_R, and ε_T are incident strain, reflected strain, and transmitted strain, respectively.

The peak load $P(t)_{max}$ and strain rate $\dot{\varepsilon}(t)$ of the specimen during impact splitting are determined using the "three-wave method" as outlined below:

$$P(t)_{max} = EA_e\varepsilon_T(t)_{max}, \tag{2}$$

$$\dot{\varepsilon}(t) = -\frac{2C_e}{D}\varepsilon_R(t). \tag{3}$$

where D is the diameter of the specimen. A_e is the cross-sectional area of the input bar and the transmission bar. E is the elastic modulus of the input bar and the transmission bar. C_e is the wave speed in the elastic rod, which is 5,190 m/s.

2.3. Test Scheme and Results. Dynamic splitting tests were conducted on sandstone CCBD specimens to investigate the dynamic tensile mechanical behavior and fracture mechanical characteristics of sandstone under the combined influence of two factors: the fissure angle θ and strain rate $\dot{\varepsilon}$ between the loading direction and the preset fracture plane. Five fissure angle θ were chosen, namely 0°, 30°, 45°, 60°, and 90°. Different levels of impact pressure (0.2, 0.3, and 0.5 MPa) were applied to achieve varying strain rates during loading conditions. The strain rate corresponds to the average value of the reflected stress wave platform segment, as shown in Figure 3. Specifically, at an impact pressure of 0.2 MPa, the strain rate ranges from 104.07 to 116.04 s^{-1}. Under an impact pressure of 0.3 MPa, the strain rate ranges from 148.55 to 168.16 s^{-1}, while under a higher impact pressure of 0.5 MPa, the strain rate ranges from 216.53 to 234.03 s^{-1} accordingly. Figure 4 illustrates the relationship between emission pressure and strain rate, demonstrating a positive correlation during loading. In this study, three identical impact tests were conducted with consistent impact pressure and crack inclination for a total of 45 experiments performed in order to ensure reliability and accuracy of results obtained. Some of the test data used in this study comes from the author's research during the doctoral period (refer to Table 2 for representative values selected).

3. Test Result Analysis

3.1. Analysis of Failure Pattern. Figure 5 shows the final failure states of sandstone CCBD specimens under three typical impact pressures p. The sandstone samples with varying fissure angles θ demonstrate distinct final failure modes under these three types of impact pressure loading conditions. Based on the damage and degree of damage to the specimens, the final failure mode has been simplified into the following three cases, as shown in Figure 6:

(1) The compound failure mechanism (Type I) is characterized by the occurrence of tensile splitting failure along the crack tip and the development of shear failure from the loading point of the specimen to the crack tip. This failure mechanism is observed as a direct crack through the crack and a pair of secondary cracks resembling the shape of "8".

(2) The composite failure mechanism (Type II) involves shear failure along the crack tip and shear tensile failure from the loading point of the specimen to the crack tip. Specifically, when the end of the prefabricated crack deviates at a certain angle from the direction of crack extension, a pair of wing-like cracks propagate steadily towards the direction of maximum principal stress. This propagation leads to the formation of a quasi-coplanar secondary crack along the same direction as the prefabricated crack. This phenomenon occurs due to the inability of plastic yield zone recovery in unloaded specimens, resulting in fracture caused by compressive-shear composite stress during unloading.

(3) The compound failure mechanism (Type III) is characterized by the occurrence of tensile failure along the middle of the specimen and shear failure developing

Table 2: Dynamic split test results of CCBD sandstone specimen [41].

Specimen number	Fissure angle, θ (°)	Impact pressure, p (MPa)	Strain rate, $\dot{\varepsilon}$ (s^{-1})	Peak load, P (KN)	Peak load time, t_p (μs)	Type I stress intensity factor, K_I^d (KPa·$m^{0.5}$)	Type I stress intensity factor, K_{II}^d (KPa·$m^{0.5}$)	Dynamic fracture toughness, K_{eff}^d (KPa·$m^{0.5}$)
FA1-1	0	0.2	106.24	19.24	52.5	2.09	0.00	2.09
FB1-1	30	0.2	113.97	17.98	43.2	−0.66	3.38	3.44
FC1-3	45	0.2	116.04	24.35	43.5	−3.73	5.00	6.24
FD1-2	60	0.2	109.71	26.22	48.4	−5.58	3.66	6.67
FE1-3	90	0.2	104.07	20.98	47.7	−5.69	0.00	5.69
FA2-2	0	0.3	148.55	38.96	31.8	4.25	0.00	4.25
FB2-3	30	0.3	168.16	32.97	38.0	−1.22	6.33	6.45
FC2-2	45	0.3	164.21	30.34	40.9	−4.51	6.02	7.52
FD2-2	60	0.3	156.88	24.73	34.1	−5.16	3.38	6.17
FE2-2	90	0.3	160.21	28.85	41.9	−7.65	0.00	7.65
FA3-2	0	0.5	216.53	52.45	39.4	5.76	0.00	5.76
FB3-2	30	0.5	230.95	43.83	35.7	−1.73	8.81	8.98
FC3-1	45	0.5	232.99	37.09	42.3	−5.82	7.70	9.65
FD3-3	60	0.5	234.03	35.96	38.9	−7.75	5.04	9.24
FE3-1	90	0.5	230.05	34.47	41.2	−9.14	0.00	9.14

from the loading point of the specimen to the crack tip. Specifically, this failure mechanism is manifested as the generation of splitting cracks through the loading path of the specimen, and a pair of quasi-coplanar secondary cracks propagate through the specimen along the preset crack direction.

When the impact pressure p is 0.2 MPa and the fissure angle θ is 0°, the failure mode of sandstone is simplified to Type I, where the upper part of the specimen fails due to continuous loading after radial fracture occurs, resembling the failure mechanism observed in curved beams. For fissure angles θ of 30° and 45°, the failure mode can be simplified to Type II. For fissure angles θ of 60° and 90°, the failure mode can be simplified to Type III. When the impact pressure p is 0.3 MPa and the fissure angle θ is 0°, the failure mode of sandstone is simplified as Type I. When the fissure angle θ is 30°, 45°, and 60°, the failure mode of sandstone is simplified as Type II. When the fissure angle θ is 90°, the failure mode of sandstone can be simplified as Type III. When the impact pressure p is 0.5 MPa and the fissure angle θ is 0°, the failure mode of sandstone is simplified to Type I. When the fissure angle θ is 30° and 45°, the failure mode of sandstone can be simplified as Type II. When the fissure angle θ is 60° and 90°, the failure mode of sandstone can be simplified as Type III. It is evident that the determination of sandstone failure mode heavily relies on the fissure angle, with minimal influence from changes in strain rate. In other words, variations in the strain rate minimally affect the impact fracture mode of specimens compared to the significant impact of fissure angle on sandstone failure mode.

3.2. Stress Wave Analysis. Figure 7 Illustrates the stress wave waveform curves of specimens with varying fissure angles under three different levels of impact pressure loading. It is evident that, at the same impact pressure, the transmitted wave curve exhibits a consistent variation pattern for specimens with different crack inclinations, characterized by either a "double peak" or "single peak" waveform. Consequently, the waveform curve is simplified as depicted in Figure 7(d), and four distinctive points (O, A, B, and C) on the transmission wave are identified. Point O represents the initiation time of transmission wave generation, point A signifies the occurrence of the first peak in the transmission wave curve, point C indicates the generation of the second peak in the transmission wave curve, while point B represents the time interval between these two peaks.

When θ is 0° and 30°, the transmitted wave of the specimen exhibits a "double peak" phenomenon. Upon application of an impact load, the stress level rapidly escalates to reach its maximum point (point A), with damage originating from the crack tip. Subsequently, as the specimen enters the unloading stage, it remains partially intact with residual bearing capacity. Consequently, further loading induces secondary compression on this remaining portion leading to a second wave peak (point C) that is lower than the initial peak. Ultimately, complete fracture occurs in the specimen causing transmission amplitude to drop to zero. This phenomenon occurs due to the presence of a large-scale crack that blocks the incident wave generated when the specimen is subjected to an impact load. In such cases, a significant proportion of energy gets diffracted along the direction of the crack, owing to a substantial impedance difference at the rock-air interface [42]. Consequently, crack initiation takes place at the tip of this obstructing crack. Simultaneously, another portion of energy propagates through the crack and reflects at the interface with the test-transmission bar, resulting in tension waves. When $\theta > 30°$, diffraction occurs as well when the incident wave encounters multiple cracks as barriers. As a result, there is very little residual strength or even none at all in these specimens, which is reflected by their waveform exhibiting characteristics similar to those observed in "single peak" patterns.

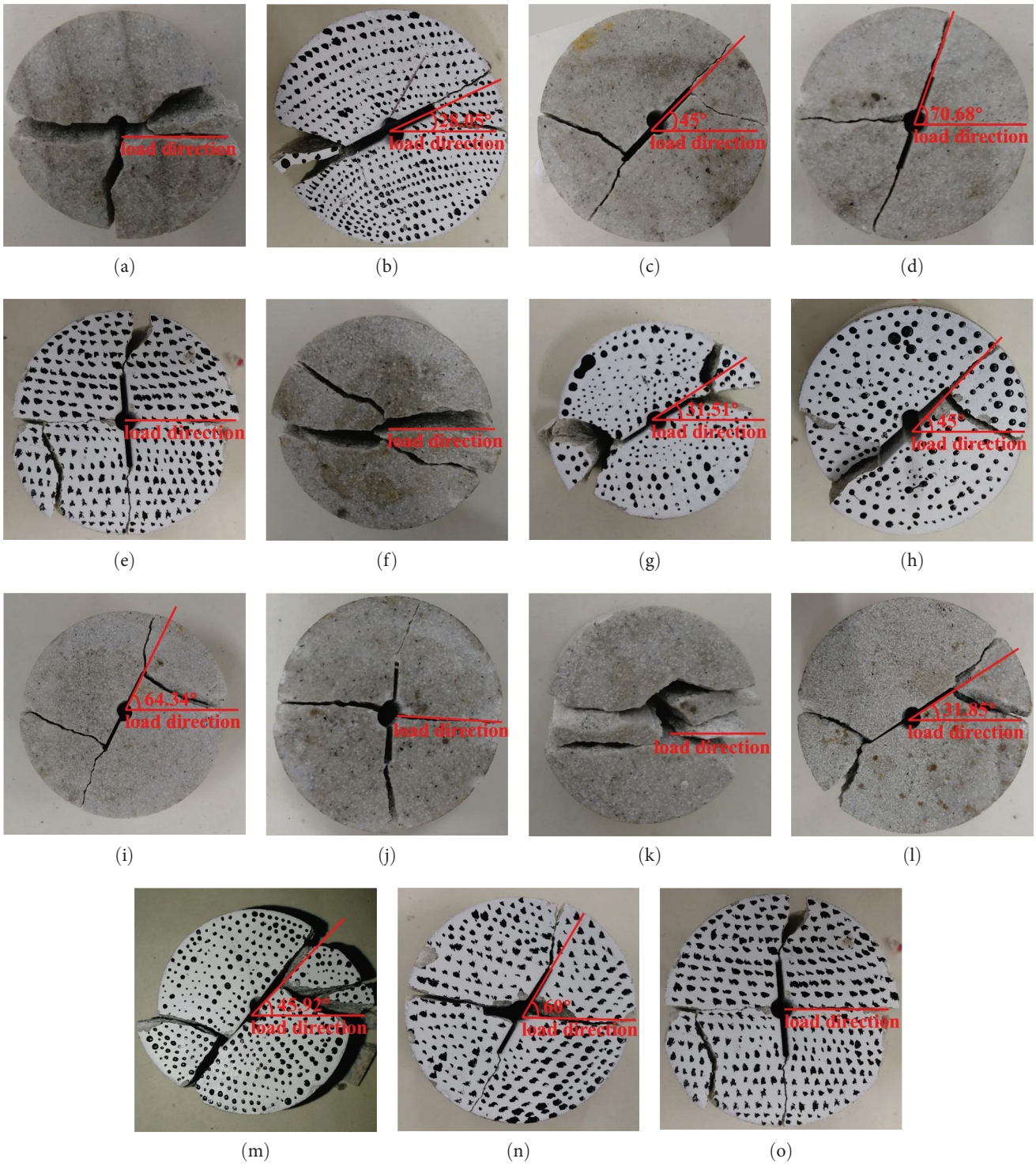

Figure 5: Failure patterns of specimen at different fissure angles and impact pressures: (a) $p = 0.2$ MPa and $\theta = 0°$, (b) $p = 0.2$ MPa and $\theta = 30°$,(c) $p = 0.2$ MPa and $\theta = 45°$, (d) $p = 0.2$ MPa and $\theta = 60°$, (e) $p = 0.2$ MPa and $\theta = 90°$, (f) $p = 0.3$ MPa and $\theta = 0°$, (g) $p = 0.3$ MPa and $\theta = 30°$,(h) $p = 0.3$ MPa and $\theta = 45°$, (i) $p = 0.3$ MPa and $\theta = 60°$, (j) $p = 0.3$ MPa and $\theta = 90°$, (k) $p = 0.5$ MPa and $\theta = 0°$, (l) $p = 0.5$ MPa and $\theta = 30°$,(m) $p = 0.5$ MPa and $\theta = 45°$, (n) $p = 0.5$ MPa and $\theta = 60°$, and (o) $p = 0.5$ MPa and $\theta = 90°$.

3.3. Dynamic Mechanical Behavior Analysis

3.3.1. Load-Radial Strain Curve Analysis. Figure 8 llustrates the load-radial strain curves of specimens with varying fissure angles under three different levels of impact pressure loading. It can be observed from the figure that the load radial strain curve of the sandstone specimen shows an increasing trend with the fissure angle θ, transitioning from a "double peak" to

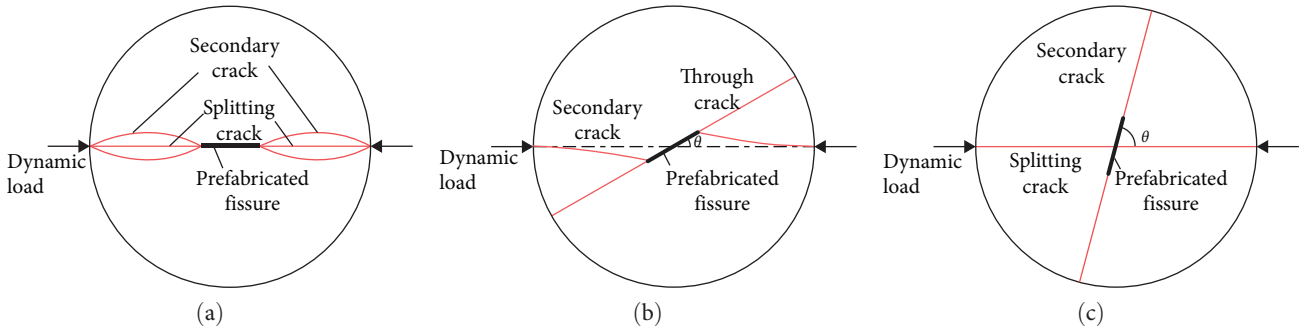

Figure 6: Typical simplified failure patterns of specimen [41]: (a) Type I, (b) Type II, and (c) Type III.

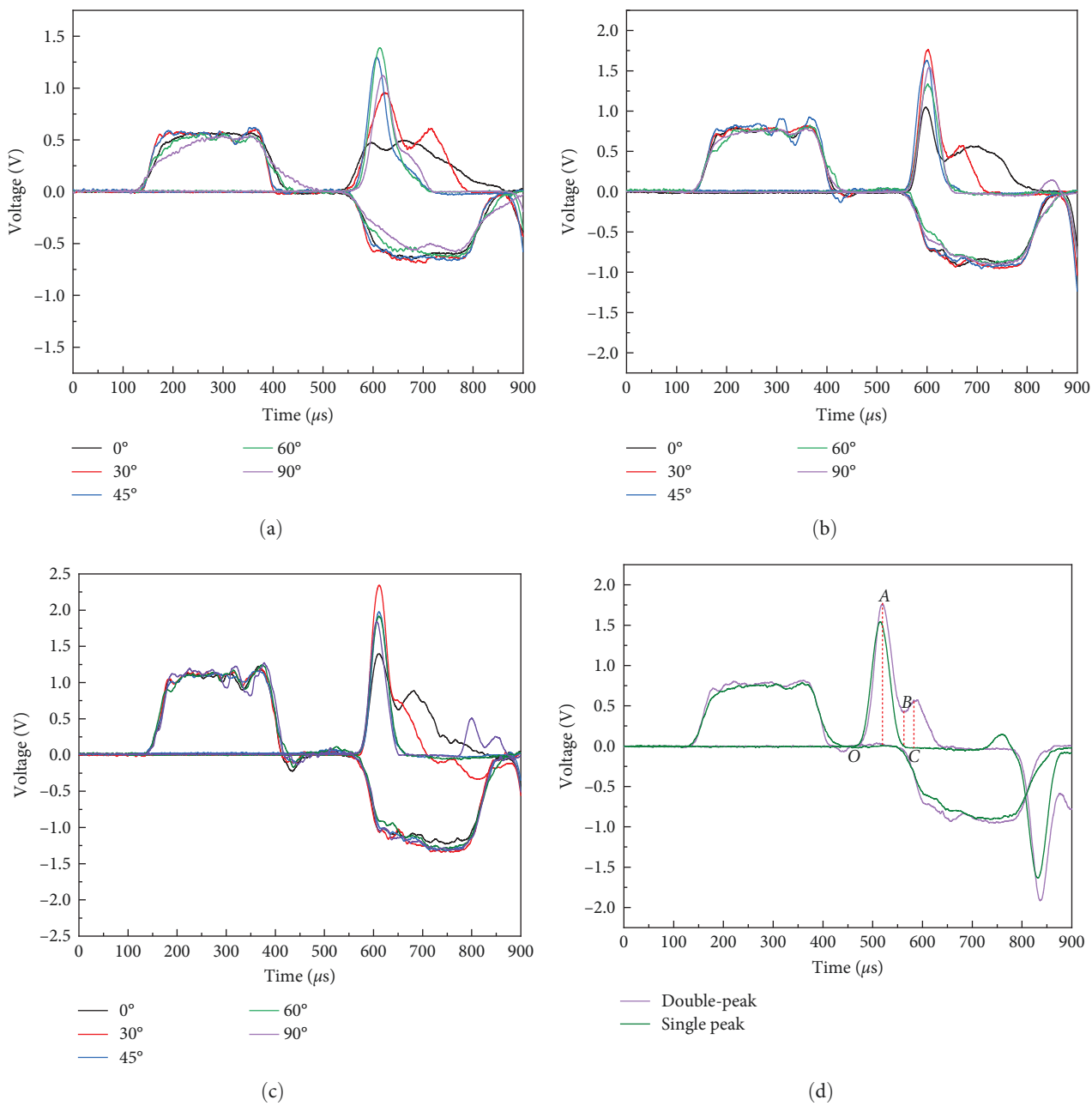

Figure 7: Waveform curves of specimen at different fissure angles and impact pressures: (a) $p = 0.2$, (b) $p = 0.3$, (c) $p = 0.5$ MPa, and (d) Simplified curve feature.

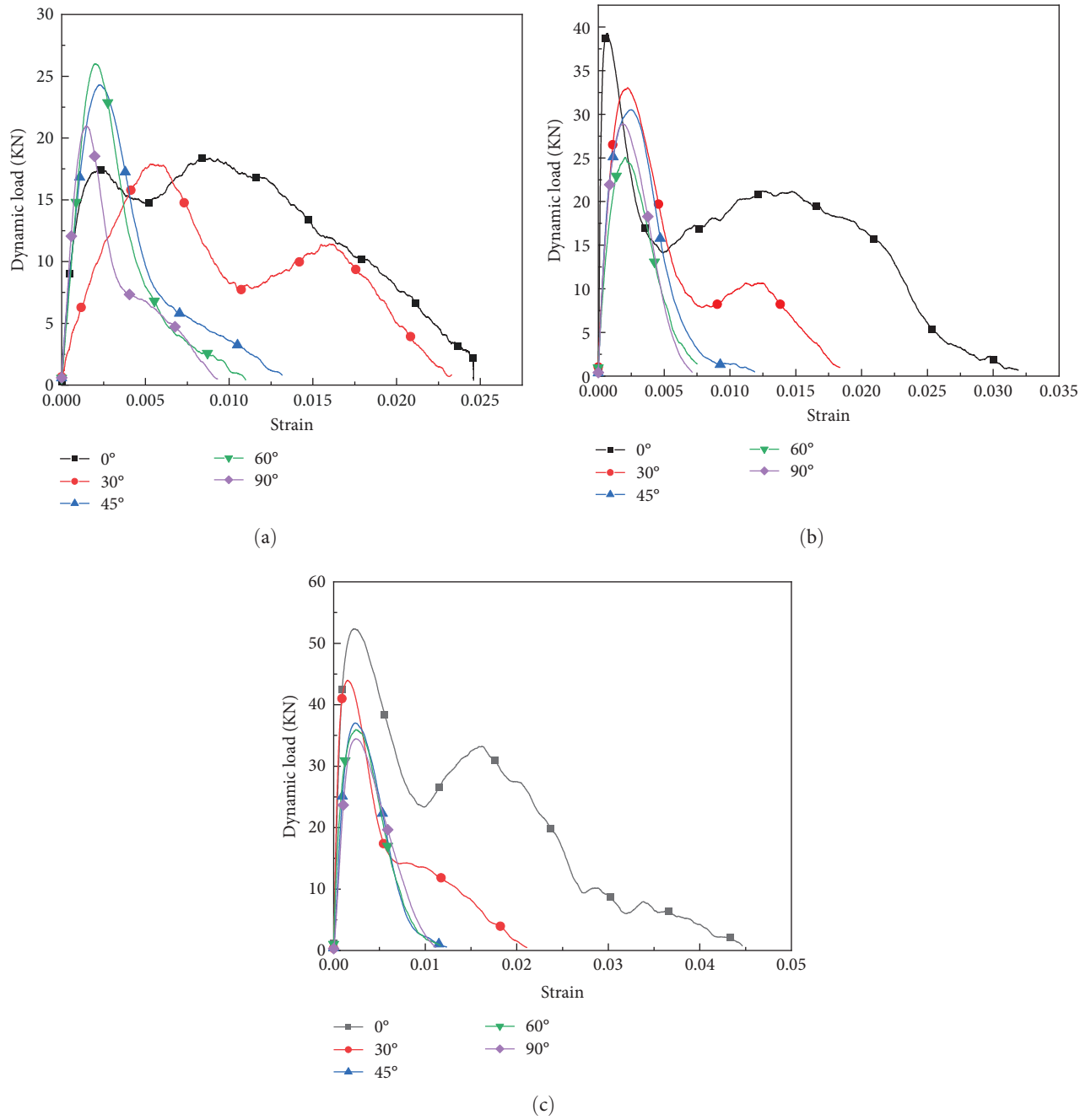

Figure 8: Load–strain responses of specimen at different fissure angles and impact pressures: (a) $p = 0.2$, (b) $p = 0.3$, and (c) $p = 0.5$ MPa.

a "single peak" type. Additionally, under identical impact pressure conditions, the time at which the peak load occurs remains approximately constant.

3.3.2. Peak Load Analysis. Figure 9 illustrates the impact of a single factor (fissure angle or strain rate) on the peak load of sandstone. In Figure 9(a), the relationship between peak load P and fissure angle θ is shown under three different impact pressure p loading conditions. It can be observed that at an impact pressure of 0.2 MPa, the trend of peak load P and fissure angle θ is more intricate: as fissure angle θ increases, the peak load P initially rises and then decreases, reaching its maximum at a fissure angle θ of 60°. Conversely, when the impact pressure p is set to 0.3 and 0.5 MPa, the peak load nonlinearly decreases with increasing fissure angle θ. Additionally, Equation (4) has been derived through fitting analysis and is represented by a solid line in the figure. The correlation coefficients R^2 for each model are measured as 0.948, 0.714, and 0.901, respectively, indicating excellent fitting performance and high reliability for all models.

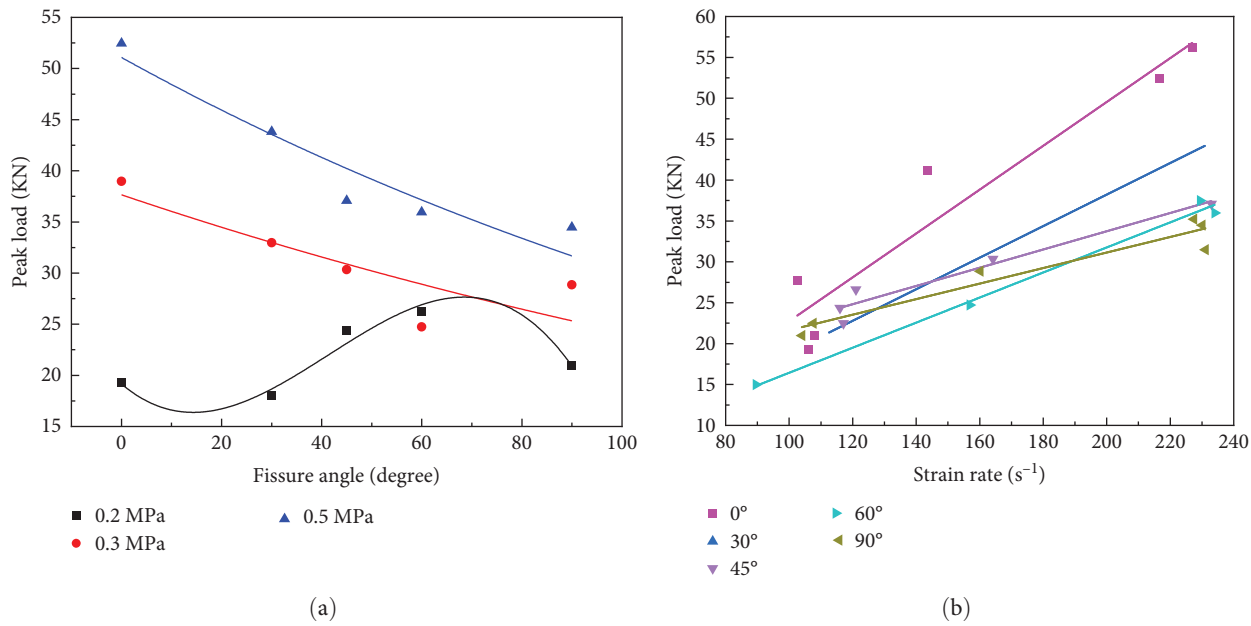

Figure 9: Influences of single factor on peak load of sandstone: (a) fissure angle and (b) strain rate.

$$P = \begin{cases} 19.16 - 0.42\theta + 0.018\theta^2 - 1.42 \times 10^{-4}\theta^3 \text{ for } p = 0.2 \text{ MPa}(R^2 = 0.948), \\ 30.88e^{-0.1478\theta} \text{ for } p = 0.3 \text{ MPa}(R^2 = 0.714), \\ 51.08e^{-0.0053\theta} \text{ for } p = 0.5 \text{ MPa}(\mathrm{R}^2 = 0.901). \end{cases} \tag{4}$$

Figure 9(b) illustrates the relationship between the peak load P and strain rate $\dot{\varepsilon}$ of sandstone with five fissure angles θ. The figure clearly demonstrates a significant dynamic enhancement effect in these sandstones. Specifically, the peak load of fractured sandstone exhibits an approximately linear correlation with the strain rate, as indicated by fitting Equation (5). The regression equations yield slopes of 0.2681, 0.1929, 0.1115, 0.1533, and 0.0950, respectively, accompanied by high correlation coefficients R^2 close to unity (0.915, 0.996, 0.945, 0.992, and 0.931, respectively), thereby confirming excellent model fitting performance and high reliability levels.

$$P = \begin{cases} 0.2681\dot{\varepsilon} - 4.096 \text{ for } \theta = 0°(R^2 = 0.915), \\ 0.1929\dot{\varepsilon} - 0.3906 \text{ for } \theta = 30°(R^2 = 0.996), \\ 0.1115\dot{\varepsilon} + 11.41 \text{ for } \theta = 45°(R^2 = 0.945), \\ 0.1533\dot{\varepsilon} + 1.081 \text{ for } \theta = 60°(R^2 = 0.992), \\ 0.0950\dot{\varepsilon} + 12.11 \text{ for } \theta = 90°(R^2 = 0.931). \end{cases} \tag{5}$$

3.4. Dynamic Fracture Toughness Analysis

3.4.1. Derivation of Dynamic Crack Initiation Criterion. Fracture toughness is a crucial parameter for assessing the fracture resistance of materials, and it can be determined as the stress intensity factor threshold based on the criterion of maximum stress intensity factor [24]. The stress intensity factor K_i (i = I, II, and III) is a fundamental physical parameter employed to characterize the mechanical state (including stress field and displacement field) at the crack tip. It is intricately linked with the dimensions, configuration, and external loading conditions of the crack. In two-dimensional stress scenarios, both K_I and K_{II} typically coexist simultaneously. For the CCBD specimen subjected to a pair of concentrated loads, K_i (i = i and II) [43–45] can be determined for the corresponding conditions based on elasticity principles.

$$K_I = \sigma\sqrt{\pi a}\left[f_{11} + 2\sum_{i=1}^{n} A_{1i} f_{1i} \alpha^{2(i-1)}\right], \tag{6}$$

$$K_{II} = 2\sigma\sum_{i=1}^{n} A_{2i} f_{2i} \alpha, \tag{7}$$

where σ is the tensile stress of the specimen, which can be calculated as $\sigma = \frac{2F}{\pi LD}$, with F representing the concentrated force received. Additionally, a denotes half the length of the preset crack and α represents the relative length of the crack, which can be calculated as $\alpha = \frac{2a}{D}$. A_{ji} and f_{ij} ($j = 1, 2$; $i = 1, 2, \ldots, n$) are variables in the general formula, as follows:

$$A_{1i}(\theta) = i\cos(2i\theta) - i\cos(2(i-1)\theta), \tag{8}$$

$$A_{2i}(\theta) = i\sin(2i\theta) - (i-1)\sin(2(i-1)\theta), \tag{9}$$

$$f_{ji} = \frac{(2i-3)!!}{(2i-2)!!}\left[1 + \frac{C_{j1}}{2i} + \frac{3C_{j2}}{4i(i+1)}\right], \tag{10}$$

where the value of coefficient n determines the calculation accuracy of K_{I} and K_{II}. The higher the value of coefficient n, the greater the calculation accuracy. In this paper, we set the value of n as 100. The general formula for coefficient C_{ji} ($j = 1, 2$; $i = 1, 2$) is as follows:

$$C_{11} = \frac{8 - 4\alpha + 3.8612\alpha^2 - 15.9344\alpha^3 + 24.607\alpha^4 - 13.234\alpha^5}{\sqrt{1-\alpha}} - 8, \tag{11}$$

$$C_{12} = \frac{-8 + 4\alpha - 0.6488\alpha^2 + 14.1232\alpha^3 - 24.2696\alpha^4 + 12.596\alpha^5}{\sqrt{1-\alpha}} + 8, \tag{12}$$

$$C_{21} = \frac{5 - 2.5\alpha + 1.4882\alpha^2 - 2.376\alpha^3 + 1.1028\alpha^4}{\sqrt{1-\alpha}} - 5, \tag{13}$$

$$C_{22} = \frac{-4 + 2\alpha + 0.4888\alpha^2 + 0.81112\alpha^3 - 0.7177\alpha^4}{\sqrt{1-\alpha}} + 4. \tag{14}$$

Based on the obtained K_{I} and K_{II}, the stress intensity factor under the type I-II composite mode can be calculated, which is called "effective stress intensity factor K_{eff}" [46, 47].

$$K_{\mathrm{eff}} = \sqrt{K_{\mathrm{I}}^2 + K_{\mathrm{II}}^2}. \tag{15}$$

To investigate the fracture behavior under different loading modes (Type I, Type II, and I–II composite modes), the stress intensity factor K_{i} (i = I, II, eff) can be determined by adjusting the angle between the interface of the sample and the loading direction for subsequent analysis.

Under dynamic loading conditions, the stress intensity factor $K_{\mathrm{I}}^{\mathrm{d}}$ (i = I, II) of the CCBD specimen represents a fundamental physical characteristic that is intricately linked to time t. Apart from being influenced by the structural composition and crack morphology, it is also significantly impacted by both the magnitude and duration of the applied load. According to the theory of one-dimensional stress waves, $K_{\mathrm{i}}^{\mathrm{d}}(t)$ (where i = I, II) can be determined under dynamic loading as follows:

$$\begin{aligned} K_{\mathrm{I}}^{\mathrm{d}}(t) &= \sigma(t)\sqrt{\pi a}\left[f_{11} + 2\sum_{i=1}^{n} A_{1i} f_{1i} \alpha^{2(i-1)}\right] \\ &= \frac{2\sqrt{\pi a} P(t)_{\max}}{\pi L D}\left[f_{11} + 2\sum_{i=1}^{n} A_{1i} f_{1i} \alpha^{2(i-1)}\right], \end{aligned} \tag{16}$$

$$K_{\mathrm{II}}^{\mathrm{d}}(t) = 2\sigma(t)\sum_{i=1}^{n} A_{2i} f_{2i} \alpha = \frac{2P(t)_{\max}}{\pi L D}\sum_{i=1}^{n} A_{2i} f_{2i} \alpha. \tag{17}$$

Table 3: Factors and levels of response variables.

Code value	Code level	Fissure angle, θ (°)	Strain rate, $\dot{\varepsilon}$ (s$-^{1}$)
X_1	−1	0	104.07
X_2	1	90	234.03

Then, the effective decay constant $K_{\mathrm{eff}}^{\mathrm{d}}(t)$ of the specimen subjected to dynamic loading is determined:

$$K_{\mathrm{eff}}^{\mathrm{d}}(\mathrm{t}) = \sqrt{\left(K_{\mathrm{I}}^{\mathrm{d}}\right)^2 + \left(K_{\mathrm{II}}^{\mathrm{d}}\right)^2}. \tag{18}$$

The dynamic crack initiation criterion of the CCBD specimen under a dynamic load can be derived as follows:

$$K_{\max}^{\mathrm{d}} > K_{\mathrm{eff}}^{\mathrm{d}}, \tag{19}$$

where $K_{\max}^{\mathrm{d}}$ represents the utmost stress intensity factor observed under dynamic loading conditions. $K_{\mathrm{eff}}^{\mathrm{d}}$ denotes the dynamic fracture toughness. In accordance with this criterion, when the maximum value of the dynamic stress intensity factor surpasses the dynamic fracture toughness, crack initiation occurs.

Based on the test data and Equations (16), (17), and (18), $K_{\mathrm{i}}^{\mathrm{d}}(t)$ (i = I, II) and $K_{\mathrm{eff}}^{\mathrm{d}}$ under dynamic load conditions were determined, with the corresponding results presented in Table 2. Multiple regression fitting was performed using Design–Expert software's Response Surface to analyze the test results, resulting in Equation (20) representing the response surface function. The influencing factors and their respective levels for the response variable are summarized in Table 3.

$$\begin{aligned} K_{\mathrm{eff}}^{\mathrm{d}} = &-1.6942 + 0.1127\theta + 0.0345\dot{\varepsilon} - 0.0001\theta\dot{\varepsilon} - 0.0006\theta^2 \\ &+ 9.43 \times 10^{-6}\dot{\varepsilon}^2. \end{aligned} \tag{20}$$

The predicted R^2 of 0.924 exhibits a reasonable level of agreement with the adjusted R^2 of 0.881, as the difference between them is <0.2. Moreover, the Adeq Precision measures at 15.59, surpassing the threshold of 4, which indicating that this model can effectively navigate the design space.

3.4.2. Reliability Analysis of Response Surface Regression Model. To validate the reliability of the function model based on the response surface, a series of rigorous analysis tests including variance analysis, residual analysis, and comparison between predicted and actual values were conducted. The results of variance analysis for the regression model are presented in Table 4. The Model f-value is 21.78 with a corresponding P-value less than 0.05, indicating statistical significance. Moreover, all three model terms (θ term, $\dot{\varepsilon}$ term, and $\theta\dot{\varepsilon}$ term) exhibit P-values below 0.05, underscoring their importance in this particular case study. The residual normal probability distribution

Table 4: Analysis of variance with regression model.

Source of variation	Sum of square	Mean square	F-value	P-value
Model	62.86	12.57	21.78	<0.0001
θ	16.07	16.07	27.83	0.0005
$\dot{\varepsilon}$	35.05	35.05	60.71	<0.0001
$\theta\dot{\varepsilon}$	0.5821	0.5821	1.01	0.3415
θ^2	4.64	4.64	8.04	0.0195
$\dot{\varepsilon}^2$	0.0037	0.0037	0.0065	0.9377
Residual	5.20	0.5773	—	—
Cor total	68.06	—	—	—

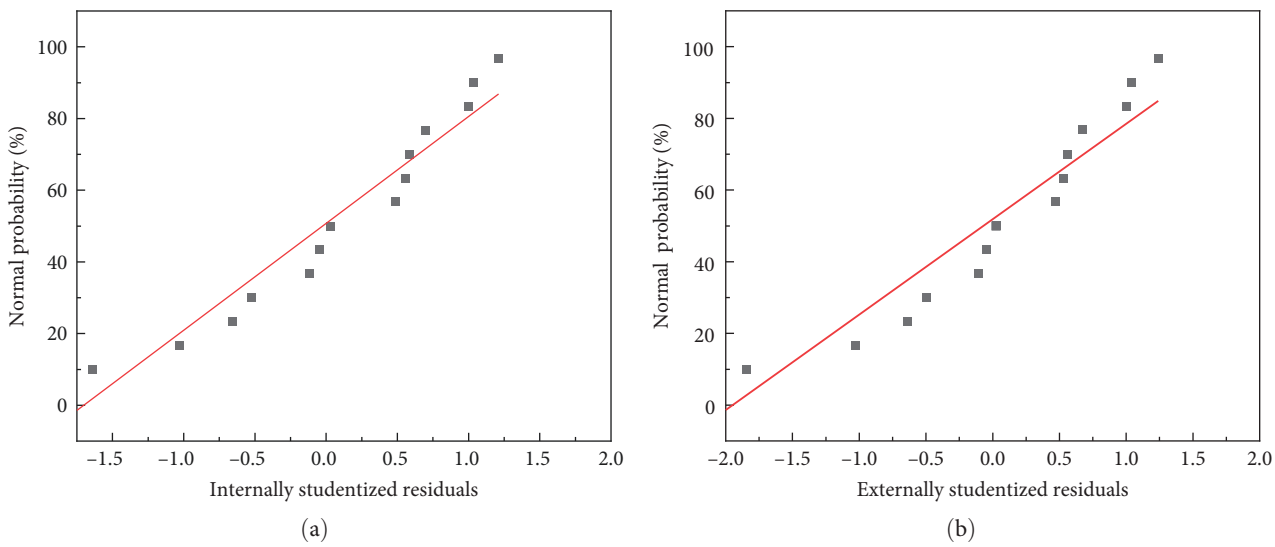

Figure 10: Residuals normal distribution plot of response surface model: (a) internally studentized residuals and (b) externally studentized residuals.

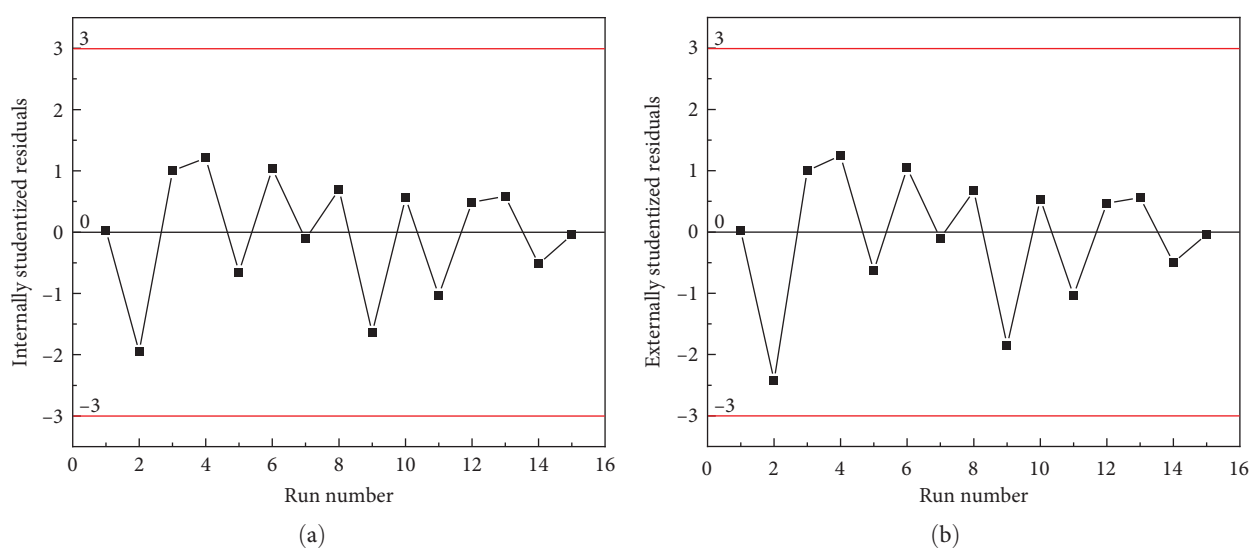

Figure 11: Residual run plot of response surface model: (a) internally studentized residuals and (b) externally studentized residuals.

diagram of sandstone dynamic fracture toughness test results is depicted in Figure 10. All points align along a straight line and are scattered without any discernible pattern, as shown in the residual operating diagram (Figure 11), indicating that the experimental data conforms to a normal distribution with no anomalous observations. Figure 12 presents a scatterplot utilizing both test and predicted values of the dynamic fracture toughness model as vertical and horizontal coordinates,

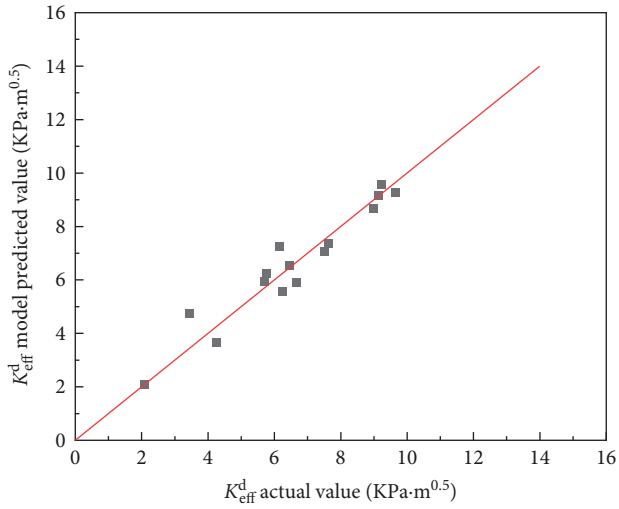

Figure 12: Comparison of predicted and experimental values of response surface model.

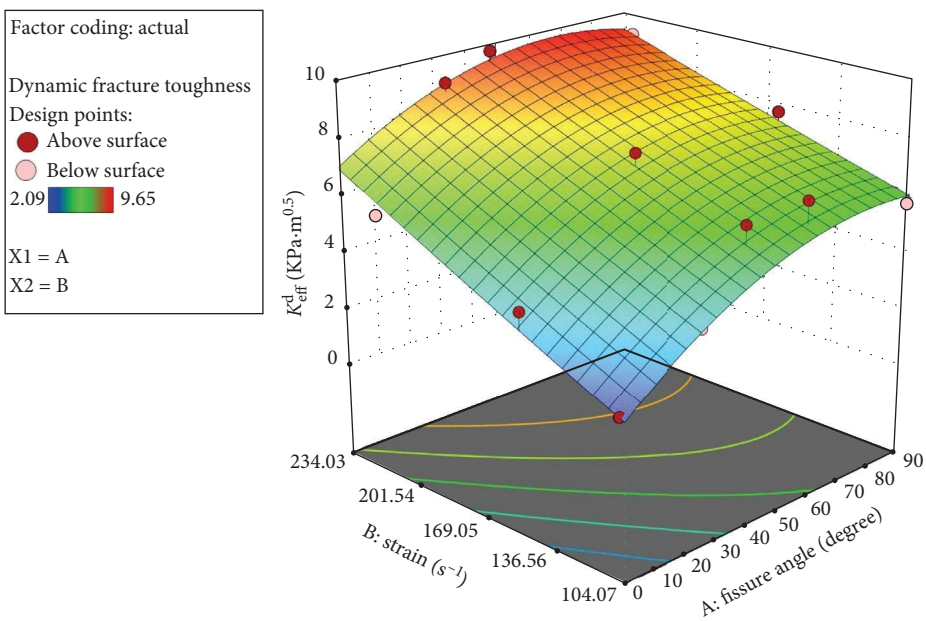

Figure 13: 3D surface graph of strain rate and fissure angle on dynamic fracture toughness of sandstone.

respectively. The predicted values from the model exhibit remarkable consistency with actual experimental results, thereby further validating the accuracy of the quadratic regression model in predicting response.

3.4.3. Dynamic Fracture Toughness Analysis. According to the variance analysis of the response surface model presented in Table 4, it is observed that among the interaction terms involving the response surface parameters, both model item θ and model item $\dot{\varepsilon}$ exhibit P values <0.001. This observation suggests that the fissure angle and strain rate $\dot{\varepsilon}$ exert significant effects on the dynamic fracture toughness of sandstone. Furthermore, it is noteworthy that the P value associated with model item $\dot{\varepsilon}$ surpasses that of model item θ, indicating a greater influence of strain rate on the dynamic fracture toughness of sandstone compared to the fissure angle.

A three-dimensional response surface is capable of directly describing the interaction between two factors and their relationship to the influence value, thereby summarizing the pattern of factor level changes on the influence value. The curvature of this surface indicates the significance of factor interactions, with greater curvature indicating a more pronounced interaction, while lesser curvature suggests less apparent effects from factors. To illustrate this concept objectively, the levels of each factor are employed as coordinates for the X and Y axis, respectively. The dynamic fracture toughness of sandstone is then used as coordinates for the Z axis, constructing a three-dimensional response surface

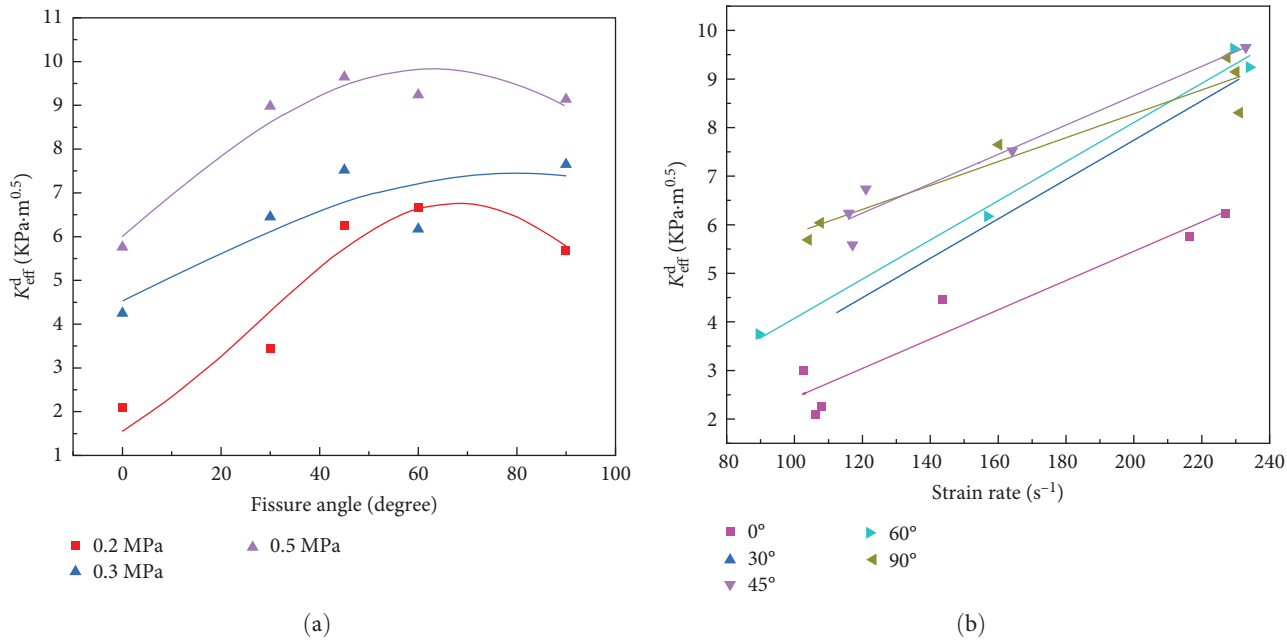

Figure 14: Influences of single factor on dynamic fracture toughness of sandstone: (a) fissure angle and (b) strain rate.

(Figure 13). Figure 13 clearly demonstrates the significant influence of both fissure angle and strain rate on the dynamic fracture toughness of sandstone. In other words, as the strain rate increases, specimens with the same fissure angle exhibit a gradual enhancement in fracture resistance. The strain rate has a positive effect on the dynamic fracture toughness, as indicated by the positive coefficient in Equation (20). The fissure angle has a positive impact on effective stress but exhibits a negative effect when the angle exceeds 60°. This implies that under identical strain rate conditions and subjected to destructive loads, sandstone attains its highest fracture resistance value at an optimal fissure angle of approximately 60°. Sensitivity analysis confirms that these findings align with subsequent experimental data regarding the effects of fissure angle and strain rate on dynamic fracture values. Based on the findings depicted in Figure 14, the impact of an individual factor on the dynamic fracture toughness of sandstone can be discerned. It is noteworthy that the trend graph obtained by altering one factor while maintaining a constant level for the other factor aligns with the pattern derived from employing the response surface method.

Based on the test results presented in Table 2, two fitting formulas (Equations (21) and (22)) have been derived that effectively capture the influence of individual factors, such as crack inclination or strain rate, on sandstone's dynamic fracture toughness. The corresponding cases exhibit correlation coefficients R^2 of 0.918, 0.745, 0.938, 0.906, 0.999, 0.925, 0.986, and 0.901, respectively, signifying a high level of reliability in the findings for each case study conducted. These equations provide detailed insights into the relationship between individual factors and sandstone's dynamic fracture toughness.

$$K_{\text{eff}}^{\text{d}} = \begin{cases} 6.757e^{-\left(\frac{\theta-67.78}{55.92}\right)^2} \text{for } p = 0.2\ \text{MPa}(R^2 = 0.918), \\ 7.451e^{-\left(\frac{\theta-79.96}{113.4}\right)^2} \text{for } p = 0.3\ \text{MPa}(R^2 = 0.745), \\ 9.824e^{-\left(\frac{\theta-62.85}{89.36}\right)^2} \text{for } p = 0.5\ \text{MPa}(R^2 = 0.938). \end{cases} \tag{21}$$

$$K_{\text{eff}}^{\text{d}} = \begin{cases} 0.0302\dot{\varepsilon} - 0.5823 \text{ for } \theta = 0^{\text{o}}(R^2 = 0.906), \\ 0.0405\dot{\varepsilon} - 0.3607 \text{ for } \theta = 30^{\text{o}}(R^2 = 0.999), \\ 0.0303\dot{\varepsilon} + 2.600 \text{ for } \theta = 45^{\text{o}}(R^2 = 0.925), \\ 0.0403\dot{\varepsilon} + 0.0454 \text{ for } \theta = 60^{\text{o}}(R^2 = 0.986), \\ 0.0246\dot{\varepsilon} + 3.364 \text{ for } \theta = 90^{\text{o}}(R^2 = 0.901). \end{cases} \tag{22}$$

4. Conclusions

(1) According to the failure forms and formation mechanisms of the specimens, the failure modes of sandstone specimens with preformed cracks under impact load can be classified into three types. The fissure angle is considered as a pivotal factor in determining the failure mode of sandstone, while the variation in strain rate has minimal influence on the impact fracture mode of specimens.

(2) Through the analysis of waveform characteristics, it is observed that under dynamic loading, when the crack inclination does not exceed 30°, the "double peak" characteristic of the transmitted wave becomes more pronounced, with the second peak lower than the first peak. However, when the crack inclination

exceeds 30°, the transmitted wave shape exhibits a form similar to a "single peak", and the diffraction law of the incident wave is identified as the primary cause for this phenomenon.

(3) The peak load of sandstone demonstrates a nonlinear decreasing trend with an increase in the fissure angle when the impact pressure is 0.3 and 0.5 MPa. However, at an impact pressure of 0.2 MPa, the peak load initially increases and then decreases, reaching its maximum value at a fissure angle of 60°. Irrespective of the type of fissure angle (CCBD specimens) under identical conditions, there is a noticeable strain rate strengthening effect as the strain rate increases.

(4) By utilizing fracture mechanics theory and one-dimensional stress wave theory, the dynamic crack initiation criterion of CCBD specimens was derived. Additionally, a regression model was established using the RSM to investigate the dynamic fracture toughness of sandstone under the combined influence of fissure angle and strain rate. Through comprehensive analysis, it was observed that the fracture resistance of sandstone is primarily governed by the strain rate, with changes in the fissure angle playing a supplementary role. Notably, as the strain rate increases, all five CCBD specimens with varying fissure angles exhibit a noticeable strengthening effect. However, when comparing similar strain rates, the findings indicate that sandstone samples possessing an internal fissure angle of 60° demonstrate superior fracture resistance.

Data Availability

All data included in this study are available upon request by contact with the corresponding author.

Conflicts of Interest

The authors declare that they have no conflicts of interest.

Acknowledgments

This work was supported by Supported by the State Key Laboratory of Precision Blasting and Hubei Key Laboratory of Blasting Engineering, Jianghan University (No. PBSKL2022D09), The Scientific Research Foundation for High-level Talents of Anhui University of Science and Technology (13210614), and the Natural Science Research Project of Anhui Educational Committee, China (2022AH052997).

References

[1] M. Amiri, H. Bakhshandeh Amnieh, M. Hasanipanah, and L. Mohammad Khanli, "A new combination of artificial neural network and K-nearest neighbors models to predict blast-induced ground vibration and air-overpressure," *Engineering with Computers*, vol. 32, no. 4, pp. 631–644, 2016.

[2] M. Ramulu, A. K. Chakraborty, and T. G. Sitharam, "Damage assessment of basaltic rock mass due to repeated blasting in a railway tunnelling project—a case study," *Tunnelling and Underground Space Technology*, vol. 24, no. 2, pp. 208–221, 2009.

[3] F. Cao, S. Zhang, and T. H. Ling, "Blasting-induced vibration response of the transition section in a branching-out tunnel and vibration control measures," *Advances in Civil Engineering*, vol. 2020, Article ID 6149452, 11 pages, 2020.

[4] Z. Zhang, C. Zhou, A. Remennikov, T. Wu, S. Lu, and Y. Xia, "Dynamic response and safety control of civil air defense tunnel under excavation blasting of subway tunnel," *Tunnelling and Underground Space Technology*, vol. 112, Article ID 103879, 2021.

[5] B. Zhu, N. Jang, C. B. Zhou, and T. Y. Wu, "Effect of excavation blast vibration on adjacent buried gas pipeline in a foundation pit," *Journal of Vibration and Shock*, vol. 39, no. 11, pp. 201–208, 2020.

[6] C. Zou, J. A. Moore, M. Sanayei, Z. Y. Tao, and Y. M. Wang, "Impedance model of train-induced vibration transmission across a transfer structure into an over track building in a metro depot," *Journal of Structural Engineering*, vol. 148, no. 11, Article ID 04022187, 2022.

[7] Q. Liu, X. Li, X. Zhang, Y. Zhou, and Y. F. Chen, "Applying constrained layer damping to reduce vibration and noise from a steel-concrete composite bridge: an experimental and numerical investigation," *Journal of Sandwich Structures & Materials*, vol. 22, no. 6, pp. 1743–1769, 2020.

[8] Q. Liu, D. J. Thompson, P. Xu, Q. Feng, and X. Li, "Investigation of train-induced vibration and noise from a steel-concrete composite railway bridge using a hybrid finite element-statistical energy analysis method," *Journal of Sound and Vibration*, vol. 471, Article ID 115197, 2020.

[9] C. Zou, Y. Wang, J. A. Moore, and M. Sanayei, "Train-induced field vibration measurements of ground and over-track buildings," *Science of the Total Environment*, vol. 575, pp. 1339–1351, 2017.

[10] C. Zou, Y. Wang, P. Wang, and J. Guo, "Measurement of ground and nearby building vibration and noise induced by trains in a metro depot," *Science of the Total Environment*, vol. 536, pp. 761–773, 2015.

[11] C. He, S. Zhou, and P. Guo, "Mitigation of railway-induced vibrations by using periodic wave impeding barriers," *Applied Mathematical Modelling*, vol. 105, pp. 496–513, 2022.

[12] L. He and Z. Tao, "Building vibration measurement and prediction during train operations," *Buildings*, vol. 14, no. 1, Article ID 142, 2024.

[13] K. Wu, Y. Zheng, S. C. Li, J. Sun, Y. C. Han, and D. X. Hao, "Vibration response law of existing buildings affected by subway tunnel boring machine excavation," *Tunnelling and Underground Space Technology*, vol. 120, Article ID 104318, 2022.

[14] Z. Lu, X. Wang, H. Teng, X. Guan, C. Song, and G. Fan, "Rock-breaking laws of disc cutters with different height differences in hard rock strata," *Advances in Civil Engineering*, vol. 2022, Article ID 2282830, 11 pages, 2022.

[15] M. Namli and F. Aras, "Investigation of effects of dynamic loads in metro tunnels during construction and operation on existing buildings," *Arabian Journal of Geosciences*, vol. 13, no. 11, pp. 1–11, 2020.

[16] J. Qiu, C. Zhou, Z. Wang, and F. Feng, "Dynamic responses and failure behavior of jointed rock masses considering pre-existing joints using a hybrid BPM-DFN approach," *Computers and Geotechnics*, vol. 155, Article ID 105237, 2023.

[17] S. S. Wang, S. Q. Yang, W. L. Tian, and Y. H. Huang, "Research on phase-field simulation method of crack propagation of rock with pre-existing fissures," *Chinese Journal*

of Rock Mechanics and Engineering, vol. 42, no. 2, pp. 365–377, 2023.

[18] C. Zhou, C. Xu, M. Karakus, and J. Shen, "A particle mechanics approach for the dynamic strength model of the jointed rock mass considering the joint orientation," *International Journal for Numerical and Analytical Methods in Geomechanics*, vol. 43, no. 18, pp. 2797–2815, 2019.

[19] H. Shi, W. Chen, H. Zhang, and L. Song, "A novel obtaining method and mesoscopic mechanism of pseudo-shear strength parameter evolution of sandstone," *Environmental Earth Sciences*, vol. 82, no. 2, Article ID 60, 2023.

[20] X. Xie, J. Li, and Y. Zheng, "Experimental study on dynamic mechanical and failure behavior of a jointed rock mass," *International Journal of Rock Mechanics and Mining Sciences*, vol. 168, Article ID 105415, 2023.

[21] T. Zhou, J. Chen, H. Xie, C. Zhou, F. Wang, and J. Zhu, "Failure and mechanical behaviors of sandstone containing a pre-existing flaw under compressive-shear loads: insight from a digital image correlation (DIC) analysis," *Rock Mechanics and Rock Engineering*, vol. 55, no. 7, pp. 4237–4256, 2022.

[22] Q. Zheng, J. Qian, H. Zhang, Y. Chen, and S. Zhang, "Velocity tomography of cross-sectional damage evolution along rock longitudinal direction under uniaxial loading," *Tunnelling and Underground Space Technology*, vol. 143, Article ID 105503, 2024.

[23] H. Shi, W. Chen, H. Zhang et al., "Dynamic strength characteristics of fractured rock mass," *Engineering Fracture Mechanics*, vol. 292, Article ID 109678, 2023.

[24] G. R. Irwin, "Analysis of stresses and strains near the end of a crack traversing a plate," *Journal of Applied Mechanics*, vol. 24, no. 3, pp. 361–364, 1957.

[25] P. Feng, Y. Xu, and F. Dai, "Effects of dynamic strain rate on the energy dissipation and fragment characteristics of cross-fissured rocks," *International Journal of Rock Mechanics and Mining Sciences*, vol. 138, Article ID 104600, 2021.

[26] T. Zhang, B. Liu, Z. Wei, Z. Jiao, Z. Song, and H. Zhang, "Dynamic mechanical responses and crack evolution of burst-prone coal with a single prefabricated fissure," *Theoretical and Applied Fracture Mechanics*, vol. 121, Article ID 103494, 2022.

[27] Y. Z. Yang and Z. N. Zhang, "Dynamic fracturing process of fissured rock under abrupt unloading condition: a numerical study," *Engineering Fracture Mechanics*, vol. 231, Article ID 107025, 2020.

[28] W. Wu, F. Gong, Q. Jiang, and L. He, "Fracture toughness weakening effect of high static pre-loaded CSTBD granite subjected to low frequency dynamic disturbance during the rock fracture," *Engineering Fracture Mechanics*, vol. 269, Article ID 108566, 2022.

[29] F. Zhao, Z. M. Shi, and S. B. Yu, "Fracture mechanics behaviors of fissured rock under dynamic loading: a review," *Environmental Earth Sciences*, vol. 81, no. 23, Article ID 526, 2022.

[30] F. Dai, R. Chen, M. J. Iqbal, and K. Xia, "Dynamic cracked chevron notched Brazilian disc method for measuring rock fracture parameters," *International Journal of Rock Mechanics and Mining Sciences*, vol. 47, no. 4, pp. 606–613, 2010.

[31] F. Gong, Y. Wang, and S. Wang, "The loading rate effect on the fracture toughness of marble using semicircular bend specimens," *Geofluids*, vol. 2020, Article ID 8876099, 8 pages, 2020.

[32] Y. Li, F. Dai, M. Wei, and H. Du, "Numerical investigation on dynamic fracture behavior of cracked rocks under mixed mode I/II loading," *Engineering Fracture Mechanics*, vol. 235, Article ID 107176, 2020.

[33] Z. L. Li and Q. Z. Wang, "Experimental research on effect of loading rate for dynamic fracture toughness of rock," *Chinese Journal of Geotechnical Engineering*, vol. 28, no. 12, pp. 2116–2120, 2006.

[34] Q. Z. Wang, S. Zhang, and H. P. Xie, "Rock dynamic fracture toughness tested with holed-cracked flattened Brazilian discs diametrically impacted by SHPB and its size effect," *Experimental Mechanics*, vol. 50, no. 7, pp. 877–885, 2010.

[35] M. Ni, K. Wang, and Q. Z. Wang, "Experimental study on mixed-mode dynamic fracture of four rocks under impact loading using Split Hopkinson Pressure Bar," *Chinese Journal of Applied Mechanics*, vol. 27, no. 4, pp. 697–702, 2010.

[36] Y. Q. Lu, S. Zhang, M. Z. Gao et al., "Experimental study on energy dissipation of dynamic fracture characteristics of P-CCNBD rock specimens under multiple stress waves," *Chinese Journal of Rock Mechanics and Engineering*, vol. 37, no. 5, pp. 1106–1114, 2018.

[37] G. Gao, W. Yao, K. Xia, and Z. Li, "Investigation of the rate dependence of fracture propagation in rocks using digital image correlation (DIC) method," *Engineering Fracture Mechanics*, vol. 138, pp. 146–155, 2015.

[38] H. Shi, L. Song, W. Chen et al., "New non-destructive method for testing the strength of cement mortar material based on vibration frequency of steel bar: theory and experiment," *Construction and Building Materials*, vol. 262, Article ID 120931, 2020.

[39] H. Shi, W. L. Chen, L. Song, and M. Li, "Pull-out debonding characteristics of rockbolt with prefabricated cracks in rock: a numerical study based on particle flow code," *Computational Particle Mechanics*, vol. 11, pp. 29–53, 2023.

[40] H. Shi, L. Song, H. Zhang et al., "Experimental and numerical studies on progressive debonding of grouted rock bolts," *International Journal of Mining Science and Technology*, vol. 32, no. 1, pp. 63–74, 2022.

[41] J. H. Wu, *Study on tensile properties of prefabricated defect sandstone under high strain rate*, Ph.D.thesis, Anhui University of Science and Technology, Huainan, China, 2014.

[42] K. P. Han and X. P. Zeng, "Using boundary-element numeric simulation to prove Hudson fractural medium theory," *Oil Geophysical Prospecting*, vol. 41, no. 5, pp. 534–540, 2006.

[43] C. Atkinson, R. E. Smelser, and J. Sanchez, "Combined mode fracture via the cracked Brazilian disk test," *International Journal of Fracture*, vol. 18, no. 4, pp. 279–291, 1982.

[44] S. M. Dong, Y. Wang, and Y. M. Xia, "Stress intensity factors of the central cracked disk subjected to concentrated load," *Journal of University of Science and Technology of China*, vol. 33, no. 3, pp. 61–68, 2003.

[45] W. Hua, S. M. Dong, and J. G. Xu, "Experimental research on fracture toughness of rust stone under mixed mode loading conditions," *Rock and Soil Mechanics*, vol. 37, no. 3, pp. 753–758, 2016.

[46] M. R. Ayatollahi and M. R. M. Aliha, "Fracture toughness study for a brittle rock subjected to mixed mode I/II loading," *International Journal of Rock Mechanics and Mining Sciences*, vol. 44, no. 4, pp. 617–624, 2007.

[47] T. Guo, K. Liu, S. Ma et al., "Dynamic fracture behavior and fracture toughness analysis of rock-concrete bi-material with interface crack at different impact angles," *Construction and Building Materials*, vol. 356, Article ID 129286, 2022.